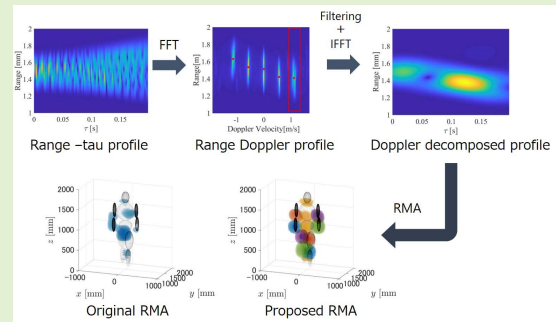


Doppler Velocity Enhanced Range Migration Algorithm for High Resolution and Noise-Robust Three-Dimensional Radar Imaging

Tomoki Ohmori and Shouhei Kidera¹, *Member, IEEE*

Abstract—Millimeter-wave and microwave short-range radar are among the most promising environmental sensing methods, with applications to situations that are otherwise optically invisible. This paper presents a Doppler velocity-enhanced range migration algorithm (RMA) that achieves both high spatial resolution and low-complexity three-dimensional (3-D) radar imaging. In this method, we address the problem of human body recognition with motion using the assumption that the motion of different human parts generates distinct micro-Doppler variations in the radar data. These variations could not only separate the RMA images with different Doppler velocities in a coherent integration-based radar imaging process, but enhances a noise reduction effect by decomposing in the Doppler velocity space. To achieve a low complexity in 3-D imaging, we incorporate the RMA method and Doppler velocity-based data decomposition. The results of numerical and experimental tests on a realistic human phantom with a walking motion demonstrate that our method provides more informative and highly separated 3-D images, even in much low SNR situation.

Index Terms—Micro-doppler analysis, millimeter wave (MMW) short range radar, range migration algorithm (RMA), human motion recognition.



I. INTRODUCTION

MICROWAVE and millimeter-wave three-dimensional short-range radar is a highly in-demand technique for diverse applications, including collision avoidance in self-driving systems with optically blurred vision, penetration of concrete or smog walls to detect human survivors in rescue scenarios, and weapons or drug detection at airport and railway security checkpoint screenings [1]. For the particular issue of human body recognition, the available spatial resolution of

radar imagery is limited owing to the bandwidth or aperture length. An approach utilizing Doppler-associated radar imaging, such as [2], [3], is one of the most promising solutions for human body recognition, especially involving motions such as walking, running, or biking. These actions can be detected by exploiting the so-called micro-Doppler signatures [4]–[9], which are derived from the distinct motion of different human body parts such as arms, legs, head, or torso.

Types of 3-D radar imaging methods include the coherent integration-based method, also termed as synthetic aperture radar (SAR) (or multidimensional beamforming, or delay and sum (DAS)) [10], [11], Kirchhoff migration [12], the range migration algorithm (RMA) [13]–[17], diffraction tomography, and compressed sensing approaches [18]–[20]. To alleviate the problems caused by phase uncertainty, several incoherent approaches using a time-of-flight profile have been developed [21]–[24], represented by the term range points migration (RPM). These offer lower computational complexity by avoiding a total search of the region of interest and coherent integration processes. However, every method faces limitations in spatial resolution or accuracy when the real or synthetic aperture length is limited.

Manuscript received June 22, 2021; accepted July 15, 2021. Date of publication July 19, 2021; date of current version September 15, 2021. This work was supported by the Japan Science and Technology Agency, Precursory Research for Embryonic Science and Technology (PRESTO), Japan, under Grant JPMJPR1771. The associate editor coordinating the review of this article and approving it for publication was Dr. Ying Zhang. (Corresponding author: Shouhei Kidera.)

Tomoki Ohmori is with the Graduate School of Informatics and Engineering, The University of Electro-Communications, Tokyo 182-8585, Japan.

Shouhei Kidera is with the Graduate School of Informatics and Engineering, The University of Electro-Communications, Tokyo 182-8585, Japan, and also with Japan Science and Technology Agency (JST), PRESTO, Chiyoda 102-0076, Japan (e-mail: kidera@uec.ac.jp).

Digital Object Identifier 10.1109/JSEN.2021.3098322

To address this problem, some studies have attempted to obtain the multiple images separated by the Doppler velocity variations, and document the effectiveness of this approach. Since each human body part has a different Doppler velocity, the response from each part can be decomposed in Doppler velocity space; this can provide each decomposed RMA image by assuming certain motion attitudes. Many studies have been developed in which the reflection responses were decomposed in range-Doppler space to enhance the apparent range resolution [25]. However, several studies have exploited Doppler velocity variations for further spatial resolution improvement in radar imaging. Ram and Majumdar [26] demonstrated that Doppler velocity-based decomposition was able to relax the resolution requirements; however, this method is based on a compressed sensing scheme, which involves large computational costs. Another promising approach is the one that incorporates both the Doppler velocity analysis and the RPM method [27], where the scattering center on the target boundary, which is obtained by RPM, is uniquely associated with a Doppler velocity. However, the accuracy of these methods largely depends on the available bandwidth, namely, the range resolution. These, therefore, usually use a super-resolution technique along range and require a higher signal-to-noise ratio (SNR) to retain a sufficient level of accuracy. Additionally, when the RPM is in a multistatic configuration, it involves relatively large computational complexity compared with the monostatic configuration [28].

To resolve the above problems, this study introduces a Doppler-associated RMA method designed to attain both high spatial resolution and higher noise reduction effect, which is a novel point of this study. The RMA method is among the highest-speed 3-D imaging approaches, in which observational data are converted to a wavenumber space and are interpolated by the so-called Stolt interpolation [29]. This enables us to reduce the complexity of a computationally expensive coherent integration process by using multidimensional fast-Fourier transform (FFT) and inverse FFT (IFFT) processes. In this study, we newly introduce a Doppler velocity-decomposed-based RMA method to provide more informative image, which has not been documented in the previous scientific literature to the best of our knowledge. This method is notable for its significant advantages in terms of both high spatial resolution, as well as the ability of the decomposed radar imagery to be associated with Doppler velocity, which represents a promising approach to problems of human attitude or motion recognition when incorporated with a machine learning approach. In addition, the filtering process in the Doppler velocity space could greatly enhance a noise-robust feature, compared with that available in the original RMA. We conducted 3-D numerical tests involving both simplified and realistic human numerical phantoms to demonstrate that our proposed method offers more informative and Doppler velocity associated radar imagery even in very noisy case, compared with the traditional RMA method.

II. METHOD

A. Observation Model

This paper discusses 3-D image reconstruction, and Figure 1 shows the observation and target 3-D models.

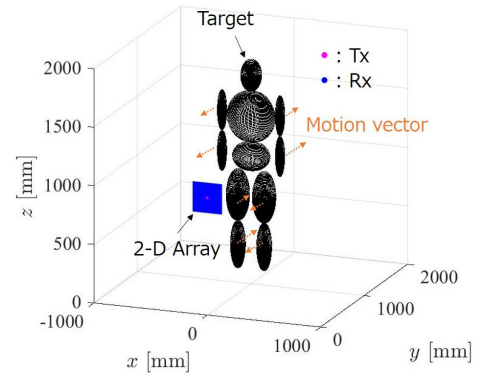


Fig. 1. Observation and target model. Magenta and blue points denote transmitters and receivers, respectively.

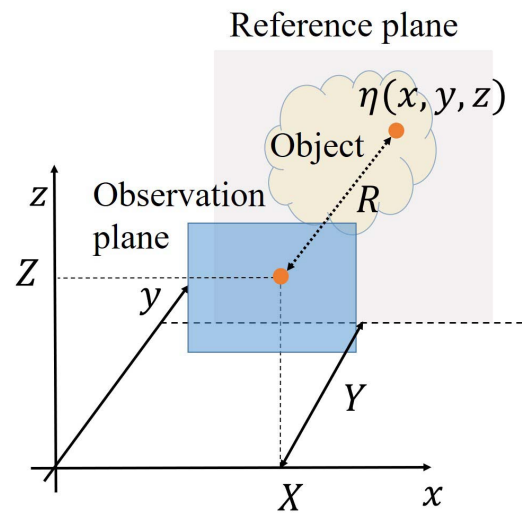


Fig. 2. Geometrical configuration in the RMA process.

A number of transmitters and receivers are arranged on the $y = 0$ plane, constituting a two-dimensional multiple-input-multiple-output (MIMO) radar, where the locations of transmitters and receivers are defined as $(X_T, 0, Z_T)$ and $(X_R, 0, Z_R)$. A pulse-modulated signal is sequentially transmitted from the transmitter with fixed PRI, where τ is defined as the time along the pulse sequence, the so-called “slow-time”. $s(X_T, Z_T, X_R, Z_R, R, \tau)$ denotes the recorded electric field of each combination of transmitter and receiver, where $R = ct/2$ is defined by a fast time t and a radio-wave velocity of c .

B. Range Migration Algorithm

For simplicity, we first introduce a mono-static based RMA model as follows, the detail of which has been described in [14]. Figure 2 shows the mono-static configuration geometry of the RMA process. Let be $\eta(x, y, z, \tau)$ the spatial profile of the reflection coefficient including the object area at the slow time τ . Let Y be the distance between the observation array plane and the reference plane as shown in Figure 2. Assuming a mono-static model, if $s(X, Z, t, \tau)$ denotes a reflection response in the time domain observed at the sensor

location denoted by $(X, 0, Z)$ with time t , which is located on the $y = 0$ plane, its Fourier response $S(X, Z, k_R, \tau)$ with $k_R = 4\omega/c$ is formulated as

$$S(X, Z, k_R, \tau) = \iiint \eta(x, y, z, \tau) \times \exp[jk_R Y] \exp[-jk_R \rho] dx dy dz, \quad (1)$$

where ρ is defined as

$$\rho = \sqrt{(x - X)^2 + (y - Y)^2 + (z - Z)^2}. \quad (2)$$

The exponential term $\exp[jk_R Y]$ denotes the phase reference at the origin of the geometry model, that is located at a distance Y from the observation plane, as shown in Fig. 2. The term $\exp[-jk_R \rho]$ presents phase rotation according to wave propagation. According to literature [14], the reflection coefficient $\eta(x, y, z, \tau)$ can be expressed as

$$\eta(x, y, z, \tau) = \iiint_{A, k_R} S(X, Z, k_R, \tau) \times \exp[jk_R(\rho - Y)] dX dZ dk_R. \quad (3)$$

where A denotes the surface of the aperture array. Since we assume that each part of the human body is located within almost the same range, the loss due to propagation and the antenna pattern are not considered for the sake of simplicity. Note that Eq. (3) is regarded a solution of the first-order Born approximation of the inverse scattering problem.

Here the triple integral in Eq. (3) can be divided into a single integral of k_R and a double integral of A as follows:

$$\eta(x, y, z, \tau) = \int_{k_R} \exp(-jk_R Y) dk_R \left\{ \iint_A S(X, Z, k_R, \tau) \times \exp(jk_R \sqrt{(x - X)^2 + (y - Y)^2 + (z - Z)^2}) dX dZ \right\} \quad (4)$$

Note that, the 2D convolution between $S(X, Z, k_R, \tau)$ and $\exp(jk_R \sqrt{x^2 + (y - Y)^2 + z^2})$ in Eq. (4), along X and Z can be computed using the complex product in the Fourier domain by introducing the 2D Fourier transform of $\exp(jk_R \sqrt{x^2 + (y - Y)^2 + z^2})$ as follows:

$$\Xi(k_X, k_Z, \tau) = \iint_A \exp(jk_R \sqrt{x^2 + (y - Y)^2 + z^2}) \times \exp[-j(k_X x + k_Z z)] dX dZ \quad (5)$$

Here, using the method of the stationary phase [30], Eq. (5) can be approximated as:

$$\Xi(k_X, k_Z, \tau) \simeq \frac{2\pi k_R}{jk_Y^2} \exp[jk_Y(Y - y)], \quad (6)$$

where k_Y denotes the wavenumber for Y . Then, substituting Eq. (6) into Eq. (5) yields the following expression of $\eta(x, y, z, \tau)$:

$$\begin{aligned} \eta(x, y, z, \tau) &\simeq \iiint_{k_X, k_R, k_Z} \frac{2\pi k_R}{jk_Y^2} S(k_X, k_Z, k_R, \tau) \\ &\times \exp(-jk_R Y) \exp[j(k_X x + k_Z z - k_Y(y - Y))] \\ &\times dk_X dk_R dk_Z, \end{aligned} \quad (7)$$

where k_X and k_Z denote the wavenumbers for X and Z , respectively, and $S(k_X, k_Z, k_R, \tau)$ denotes the 2-D Fourier transform of $s(X, Z, k_R, \tau)$ in terms of X and Z . Finally, using the relationship $k_Y = \sqrt{k_R^2 - k_X^2 - k_Z^2}$ ($k_R^2 \geq k_X^2 + k_Z^2$), the reflection coefficient proportional image $\eta(x, y, z, \tau)$ is given as follows:

$$\begin{aligned} \eta(x, y, z, \tau) &= \iiint_{k_X, k_Z, k_Y} \frac{2\pi k_R}{jk_Y^2} S(k_X, k_Z, k_Y, \tau) \\ &\times \exp(-j(k_R + k_Y)Y) \exp[j(k_X x + k_Z z - k_Y y)] \\ &\times dk_X dk_Y dk_Z, \end{aligned} \quad (8)$$

Note that, $S(k_X, k_Z, k_R, \tau)$ was resampled to $S(k_X, k_Z, k_Y, \tau)$ using the Stolt interpolation [29], and Eq. (8) implies that a spatial profile of reflectivity can be obtained via the 3-D IFFT of the product of the resampled wavenumber data as $S(k_X, k_Z, k_Y, \tau)$ and $\frac{2\pi k_R}{jk_Y^2} S(k_X, k_Z, k_Y, \tau) \exp(-j(k_R + k_Y)Y)$, this process is known as the matched filter process.

C. Doppler Velocity Decomposed RMA in Multi-Static Model

Next, we introduce the following Doppler velocity separated multi-static RMA scheme. The proposed method is based on the idea that each human body part has a different motion velocity. Note that if two objects have different Doppler velocities, their reflection responses can be decomposed in the Doppler velocity space, even if they are closely located within the azimuth and elevation angle resolutions. That is, if these responses are separated in the Doppler velocity space, the RMA image could be also decomposed by the associated Doppler velocity.

First, by assuming the multi-static observation model described in Sec. II-A, the observed signal $s(X_T, Z_T, X_R, Z_R, R, \tau)$ at each antenna combination is converted to the Doppler velocity space as:

$$\begin{aligned} S(X_T, Z_T, X_R, Z_R, R, v_d) &= \int_T s(X_T, Z_T, X_R, Z_R, R, \tau) \exp(-j\omega\tau) d\tau, \end{aligned} \quad (9)$$

where $v_d = \omega\lambda/4\pi$ and T denotes the coherent integration time. Here, using a coherently averaged responses of $S(X_T, Z_T, X_R, Z_R, R, v_d)$ for all combinations of transmitters and receivers, defined as $\tilde{S}(R, v_d)$, the Doppler velocity associated discrete point referred to as $(\tilde{R}_i, \tilde{v}_{d,i})$ is extracted by satisfying the following condition:

$$\begin{aligned} |\tilde{S}(R, v_d)|/\partial R &= 0 \\ |\tilde{S}(R, v_d)|/\partial v_d &= 0. \end{aligned} \quad (10)$$

Note that, this process is effective in the case the aperture length is much smaller than the observation distance, because the observable Doppler velocity is almost same in each combination of transmitter and receiver. Then, each decomposed

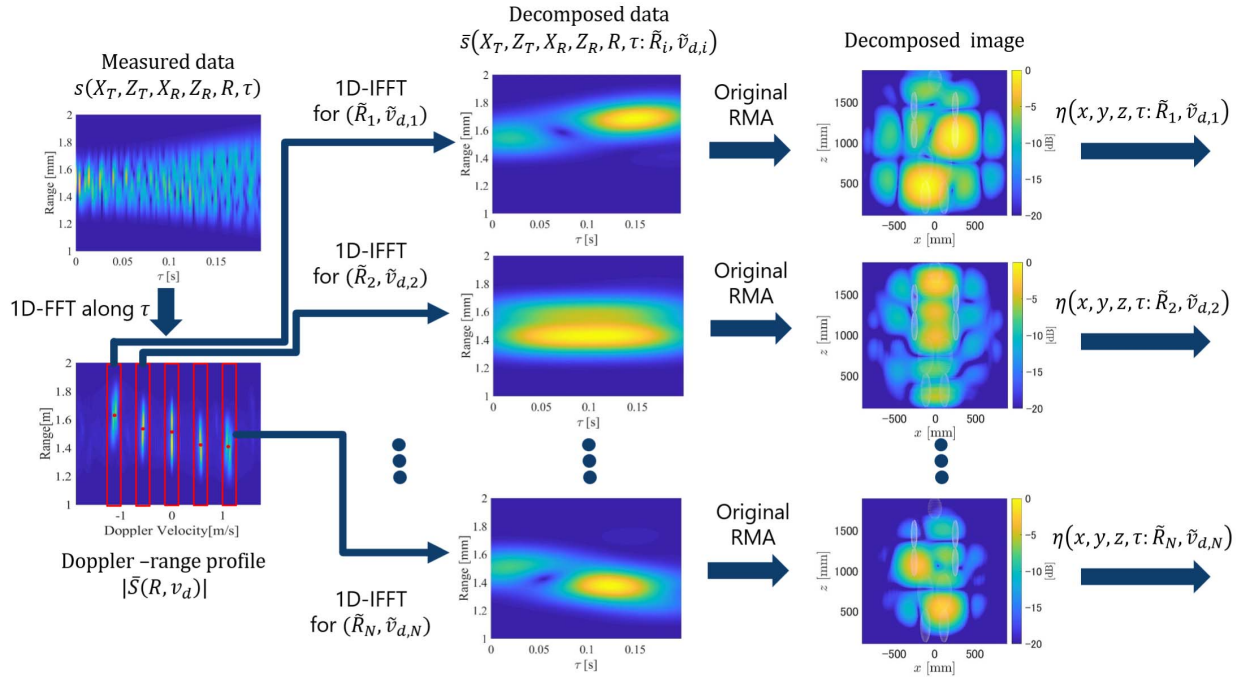


Fig. 3. Proposed scheme of Doppler velocity decomposed and associated RMA.

signal in regard to $(\tilde{R}_i, \tilde{v}_{d,i})$ is given by the following equation:

$$\begin{aligned} \tilde{s}(X_T, Z_T, X_R, Z_R, R, \tau; \tilde{R}_i, \tilde{v}_{d,i}) \\ = \frac{1}{2\pi} \int W(X_T, Z_T, X_R, Z_R, R, v_d; \tilde{R}_i, \tilde{v}_{d,i}) \\ \times S(X_T, Z_T, X_R, Z_R, R, v_d) \exp(-j\omega\tau) dv_d, \quad (11) \end{aligned}$$

where $W(X_T, Z_T, X_R, Z_R, R, v_d; \tilde{R}_i, \tilde{v}_{d,i})$ denote the windowing function on the $(X_T, Z_T, X_R, Z_R, R, v_d)$ space around $(\tilde{R}_i, \tilde{v}_{d,i})$, such as Gaussian or Hamming function, the filtering width of which should be over the Doppler velocity resolution, determined by the coherent processing interval (CPI).

Finally, for each $(\tilde{R}_i, \tilde{v}_{d,i})$, the multi-static extended RMA is applied to a decomposed signal $\tilde{s}(X_T, Z_T, X_R, Z_R, R, \tau; \tilde{R}_i, \tilde{v}_{d,i})$. Here, the mono-static based RMA is extended to the multi-static scheme by introducing the definitions $X \equiv \frac{X_R + X_T}{2}$ and $Z \equiv \frac{Z_R + Z_T}{2}$ in [15], and the following conversion is introduced:

$$\begin{aligned} \tilde{S}(X, Z, k_R, \tau; \tilde{R}_i, \tilde{v}_{d,i}) = \tilde{S}(X_T, Z_T, X_R, Z_R, k_R, \tau; \tilde{R}_i, \tilde{v}_{d,i}) \\ \times \frac{\tilde{s}_{\text{ref}}(X, Z, k_R)}{\tilde{s}_{\text{ref}}(X_T, Z_T, X_R, Z_R, k_R)}, \quad (12) \end{aligned}$$

where $\tilde{S}(X_T, Z_T, X_R, Z_R, k_R, \tau; \tilde{R}_i, \tilde{v}_{d,i})$ denote the Fourier transform of $\tilde{s}(X_T, Z_T, X_R, Z_R, R, \tau; \tilde{R}_i, \tilde{v}_{d,i})$ as to R . Also, the following definitions are introduced:

$$\tilde{s}_{\text{ref}}(X, Z, k_R) \equiv e^{-j2k_R R_C} \quad (13)$$

$$\tilde{s}_{\text{ref}}(X_T, Z_T, X_R, Z_R, k_R) \equiv e^{-jk_R(R_R + R_T)}, \quad (14)$$

where R_C denotes the distance between $(X, 0, Z)$ and the reference point target, and R_R and R_T denote the distances from the same reference point target to $(X_R, 0, Z_R)$ and

$(X_T, 0, Z_T)$, respectively. Figure 3 shows the schematic illustration of the proposed method. The figure indicates that if each Doppler velocity component can be resolved in the Doppler-range profile as $\tilde{S}(R, v_d)$, the reflection responses, such as those from the upper left and right legs, can be separated by the filtering process of Eq. (11).

D. Procedure of Proposed Method

The actual processing flow used in our proposed method is summarized below:

- Step 1) Observed data from each transmitter and receiver combination are acquired as $s(X_T, Z_T, X_R, Z_R, R, \tau)$.
- Step 2) Doppler velocity responses $S(X_T, Z_T, X_R, Z_R, R, v_d)$ are calculated using Eq. (9), and a number of discrete points $(\tilde{R}_i, \tilde{v}_{d,i})$ are extracted from local maxima of $S(X_T, Z_T, X_R, Z_R, R, v_d)$ as in Eq. (10).
- Step 3) For each $(\tilde{R}_i, \tilde{v}_{d,i})$, the filtering process shown in Eq. (11) is adopted and the Doppler decomposed scattered data given as $\tilde{s}(X_T, Z_T, X_R, Z_R, R, \tau; \tilde{R}_i, \tilde{v}_{d,i})$ are collected.
- Step 4) For each set of Doppler decomposed data, the mono-static conversion is applied as shown Eq. (12).
- Step 5) The 2-D Fourier transform is applied to $\tilde{S}(X, Z, k_R, \tau; \tilde{R}_i, \tilde{v}_{d,i})$ as:

$$\begin{aligned} \hat{S}(k_X, k_Z, k_R, \tau; \tilde{R}_i, \tilde{v}_{d,i}) \\ = \iint \tilde{S}(X, Z, k_R, \tau; \tilde{R}_i, \tilde{v}_{d,i}) \\ \times \exp[-(jk_X X + jk_Z Z)] dX dZ. \quad (15) \end{aligned}$$

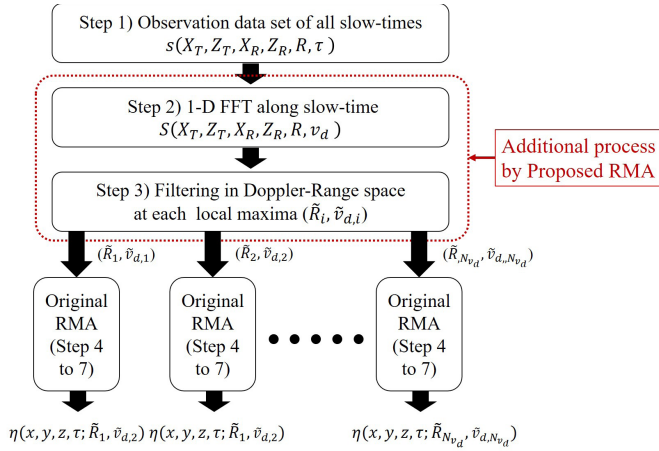


Fig. 4. Flowchart of the proposed method.

Step 6) Matched filtering [14] is applied to compensate the phase rotation to the reference plane $y = Y$ as:

$$\hat{S}_{MF}(k_X, k_Z, k_R, \tau; \tilde{R}_i, \tilde{v}_{d,i}) = \hat{S}(k_X, k_Z, k_R, \tau; \tilde{R}_i, \tilde{v}_{d,i}) \exp(jk_Y Y), \quad (16)$$

and the Stolt interpolation process is applied as:

$$\hat{S}_{MF}(k_X, k_Z, k_R, \tau; \tilde{R}_i, \tilde{v}_{d,i}) \rightarrow \hat{S}_{MF}(k_X, k_Z, k_Y, \tau; \tilde{R}_i, \tilde{v}_{d,i}), \quad (17)$$

where $k_Y = \sqrt{k_R^2 - k_X^2 - k_Z^2}$. Here, a multi-dimensional Spline interpolation algorithm is applied.

Step 7) Each Doppler separated RMA image $\eta(x, y, z, \tau; \tilde{R}_i, \tilde{v}_{d,i})$ is obtained as:

$$\begin{aligned} \eta(x, y, z, \tau; \tilde{R}_i, \tilde{v}_{d,i}) &= \iiint \hat{S}_{MF}(k_X, k_Z, k_Y, \tau; \tilde{R}_i, \tilde{v}_{d,i}) \\ &\times \exp[-j(k_R - k_Y)y] \\ &\times \exp[j(k_X x + k_Z z - k_Y y)] dk_X dk_Y dk_Z. \end{aligned} \quad (18)$$

Note that, Steps 2 and 3 correspond to the additional process derived from the original RMA, that is, Doppler velocity decomposition. Steps 4 - 7 form the original RMA process. For each filtered response $\bar{s}(X_T, Z_T, X_R, Z_R, R, \tau; \tilde{R}_i, \tilde{v}_{d,i})$, the original RMA is parallelly processed, and a number of RMA images associated with different Doppler velocities are available in the proposed method. Figure 4 shows the flowchart of the proposed method; the procedures that are common to and those that are different from the procedures in the original RMA are clearly indicated. Note that this method has the definitive advantages of being able to provide a multiple Doppler-decomposed or associated RMA images at each slow time τ , which contributes to the tracking of each human body part during the time of observation and the recognition of human body motion and attitudes.

III. NUMERICAL TESTING

Here, we describe the performance assessment of the proposed method using a simplified and realistic human numerical

TABLE I
DOPPLER VELOCITY FOR EACH PART OF HUMAN BODY

Doppler velocity	Parts
-1.0 m/s	Right lower arm & Left lower leg
-0.5 m/s	Right upper arm & Left upper leg
0 m/s	Head & Lower and Upper torso
0.5 m/s	Left upper arm & Right upper leg
1.0 m/s	Left lower arm & Right lower leg

phantom. In the first test, the simplified model is based on an aggregation of ellipsoids that mimic various parts of the human body. This enables us to assess each method in a strict and more quantitative manner in terms of the accuracy or resolution of the Doppler velocity and RMA images. In the latter test, we use a realistic model, which offers more convincing and reliable results for discussions, for an advantage or problem in extending to a real world scenario.

A. Simplified Human Model

1) *Setting*: In this test, a simplified numerical model of a human body is introduced, in which each human body part, such as the left and right arms or legs, head, and upper and lower torso, is represented by an ellipsoid as shown in 5a. A stepping motion of the human body at the same position is assumed for simplicity, and the constant Doppler velocity of each part is summarized in Table I, namely, the torso or head has zero velocity. Note that, assuming a pendulum movement for each arm or leg, a lower and upper part of them would have a different velocity in this case. One transmitter is located at the center of the planar array on the $y = 0$ plane, which contains 5×5 receivers separated by a 15 mm spacing. The total data from 25 receiving points are then processed in this model, which is referred to as single-input multiple-output (SIMO). A pulse modulated signal is transmitted from each transmitter with a 20 GHz center frequency and 0.5 GHz bandwidth, giving it a theoretical range resolution of 300 mm in air. The angular resolution is estimated at 190 mm when the distance from the array to the target is 1500 mm. We assumed a pulse radar sequence of 100 sequentially transmitted pulses from each transmitter with an equal PRI of 2 ms. The unambiguous range and the resolution of Doppler velocity are 1.5 m/s and 0.03 m/s, respectively. Because this model involves a high frequency signal, the reflection data are generated via a geometric optics (GO) approximation [31]. Note that while multiple scattering effects among human body parts are not considered, here, the effect of interference among several reflections from multiple objects is considered in the GO. Figure 5b shows the range-Doppler velocity profile, where the coherent processing interval (CPI) is 0.2 s. In this figure, the Doppler velocity of each part is clearly resolved. Note that, since the maximum displacement of each part (e.g., the lower arm or leg with 1.0 m/s velocity) along CPI is within 200 mm, which is within the theoretical range resolution (300 mm), the cross range effect that can degrade the Doppler resolution may be negligible in this case.

2) *Imaging Results*: Figure 6 shows the cross-sectional images of $S(k_X, k_Z, k_R, \tau)$, at the specific k_X , k_Z , and k_R ,

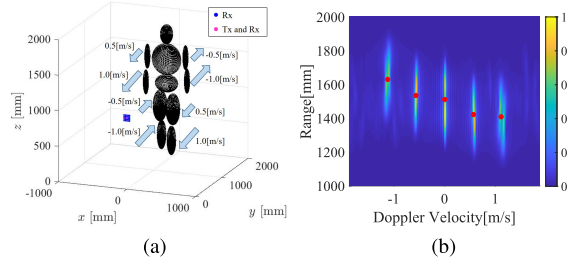


Fig. 5. (a): Simulation model with simplified human model. (b): Range Doppler velocity profile at the specific combination of transmitter and receiver.

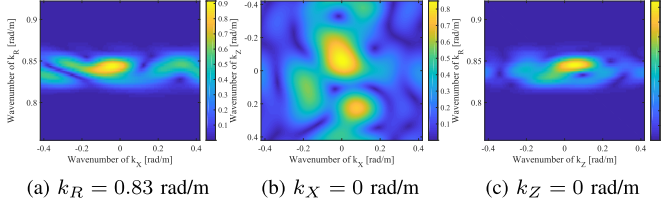


Fig. 6. Example of cross-sectional k space profiles of $S(k_X, k_Z, k_R, \tau)$ at $\tau = 100$ ms.

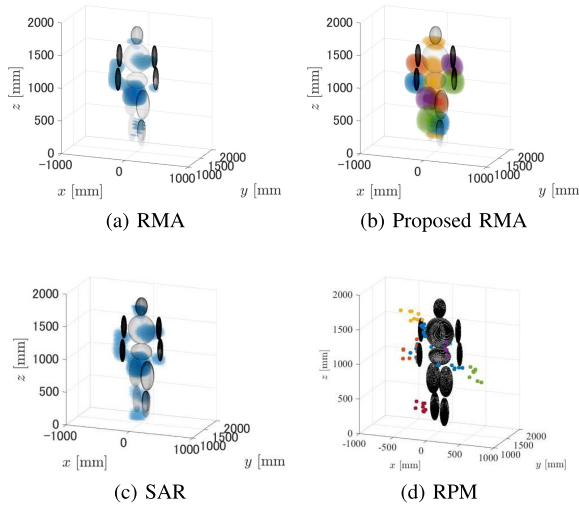
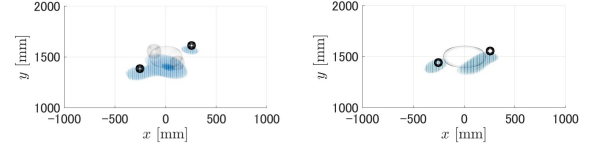


Fig. 7. Reconstruction images provided by each method at the absence of noise.

where $\tau = 100$ ms. Note that, k_X and k_Z are equivalent to the decomposition variables along the azimuth and elevation angles, respectively, and k_R denotes the frequency response of the time-domain signal. Then, $S(k_X, k_Z, k_R, \tau)$ can be regarded as the 3-D beam pattern. Figure 5b shows the range-Doppler velocity responses after coherently integrated data was obtained along the receivers, namely, $\tilde{S}(R, v_d)$, which demonstrates that each part of the Doppler velocity is clearly decomposed. Figures 7 and 8 show the reconstruction results obtained by the original RMA and the Doppler-associated RMA using the proposed method at the 3-D view and sliced images at the specific range, respectively. Note that, the Hamming window function with a width of 0.3 m/s, denoted as ΔW in the Doppler velocity direction was applied in the filtering process in Eq. (11). The results show that the original RMA



(a) Original RMA, $900\text{mm} \leq z \leq 1100\text{mm}$ (b) Original RMA, $1300\text{mm} \leq z \leq 1500\text{mm}$

(c) Proposed RMA, $900\text{mm} \leq z \leq 1100\text{mm}$ (d) Proposed RMA, $1300\text{mm} \leq z \leq 1500\text{mm}$

Fig. 8. Reconstruction images produced by the original and the proposed RMA at $\text{SNR} = \infty$. Black dots denote actual target profiles.

could not resolve certain parts of the human body with less scatters, especially the right arm, upper torso, left and right upper legs in contrast, the proposed method clearly resolves all parts of the human body by providing more scatters by via the aggregation of multiple RMA images associated with Doppler velocities. In particular, the reflection responses around a Doppler velocity of -1.0 m/s generate images of only the corresponding part of human body, *i.e.*, the right arm or left leg in this case, while those around 1.0 m/s Doppler velocity generate images of the left arm or right leg. In the original RMA image, as shown in Fig. 7(a), the left and right upper legs were not resolved owing to insufficient angular resolution; however, with the proposed method, both the left and right upper legs were imaged, as shown in Fig. 7(b), by using the decomposition in the range-Doppler velocity space in Eq. (11). For a quantitative analysis of the spatial resolution, Fig. 9 shows the 1-D cross section of the representative y and z . Focusing on the 1-D image of $z = 1600$ mm and $z = 1400$ mm, we expect to view the upper torso, and the left and right upper arms. The Doppler decomposed RMA reconstructs each part of the human body, while the original RMA cannot decompose these parts. Also, the case of $z = 950$ mm should cover three parts, namely, the lower torso and the left and right lower arms; however, the original RMA can provide only one blurred responses around the torso. In contrast, the proposed RMA offers clearly separated responses for each part of the human body. In addition, the proposed method successfully generates an associated Doppler velocity with an RMA image, thus providing a more informative method of reconstructing human body motion or for use in attitude recognition problem.

Further comparison to other methods was conducted by obtaining reconstruction results by the SAR (DAS) and the k -space-decomposed RPM methods [32], shown in Fig. 7. The SAR results generate a nearly identical image to that produced by the original RMA, and it fails to perfectly decompose each part of the human body. In contrast, the RPM

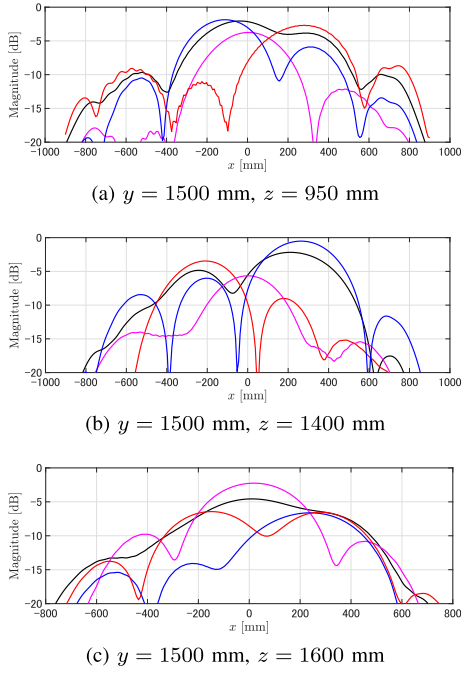


Fig. 9. Cross sectional images of reconstruction images produced by the original and the proposed RMA at $\text{SNR} = \infty$. Black solid line: Original RMA. Red, magenta, blue solid line: Proposed RMA decomposed by different Doppler velocities. Black dots denote actual target profiles, namely, ground truth.

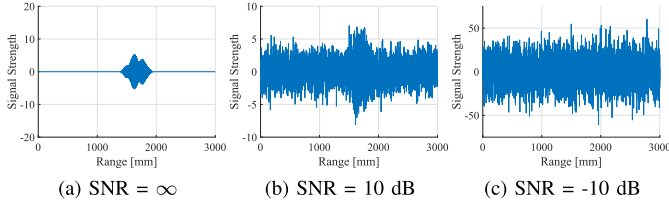


Fig. 10. Received signals in the simplified human model at different SNRs.

exhibits several scattering centers on the target body; however, some points have deviated from the actual boundary, although the k-space decomposition process results in an enhanced azimuth resolution. The computational times of each method determined using an Intel Xeon Silver 2.10-GHz 4110 CPU with 256 GB RAM are summarized in Table III. As shown in this comparison, the computational time of the proposed method is not significantly greater than that required in the original RMA method, due to the use of parallel processing. In addition, the above computational time could be significantly reduced by downsampling the pixel interval of RMA, if the real-time processing would be a top priority.

3) Sensitivity to Noise: The sensitivity to additive noise is investigated as follows, to emulate real-world operating conditions. Gaussian white noise is added to each recorded signal, where the SNR is defined as the ratio between the maximum signal power to the noise variance in the time domain. We investigate the two cases of a 10 dB and -10 dB SNRs. Figure 10 shows the examples of the received signals at each SNR level in this case. In addition, Figs. 11 and 12 illustrate the range- τ and range-Doppler data at each SNR

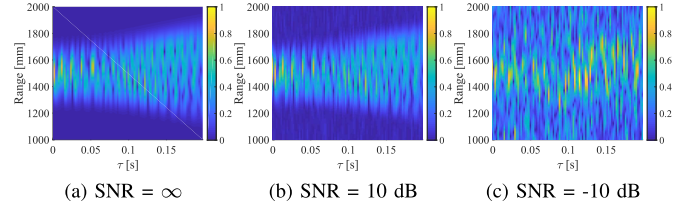


Fig. 11. Range- τ profiles in the simplified human model at different SNRs.

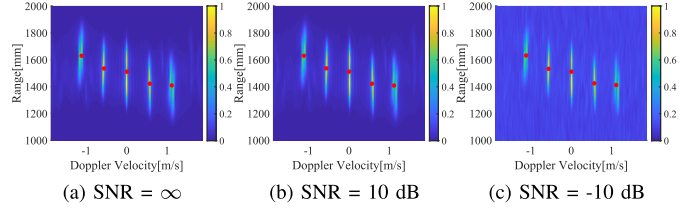


Fig. 12. Range-Doppler velocity profiles in the simplified human model at different SNRs. Red solid circles denote the extracted local maxima ($\hat{R}_i, \hat{v}_{d,i}$).

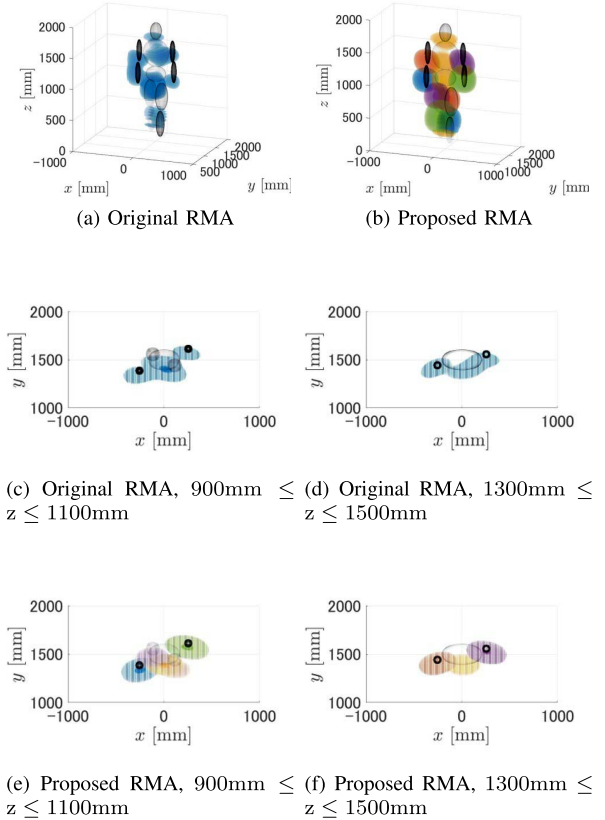


Fig. 13. Reconstruction images produced by the original and the proposed RMA at $\text{SNR} = 10$ dB. Black dots denote actual target profiles.

level, and demonstrate that our method successfully suppresses the random noise components, not only using the matched filtering processing along the R direction, but also by noise-reduction filtering in Doppler velocity space with the Step 3) process in the proposed method. The reconstruction results obtained by the RMA method without and with Doppler data decomposition are shown in Figs. 13 and 14, and these

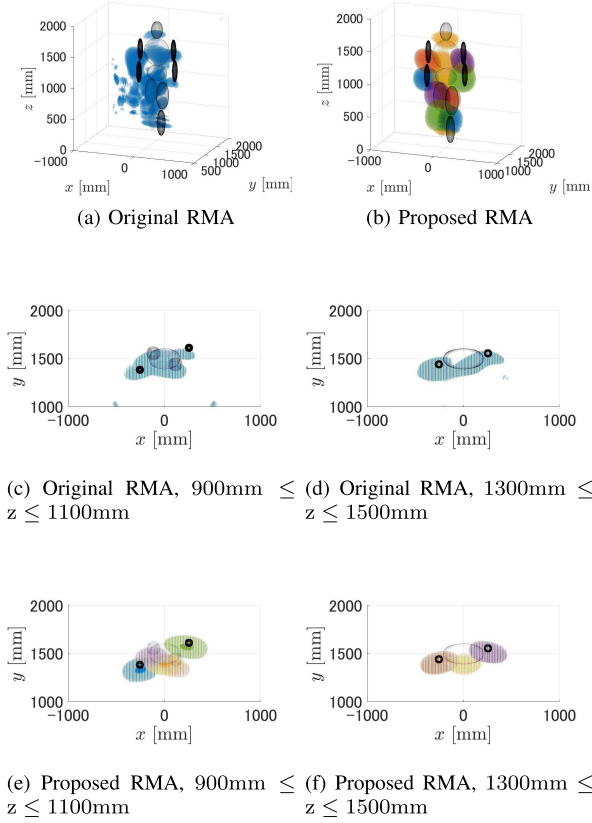


Fig. 14. Reconstruction images produced by the original and the proposed RMA at SNR = -10 dB. Black dots denote actual target profiles.

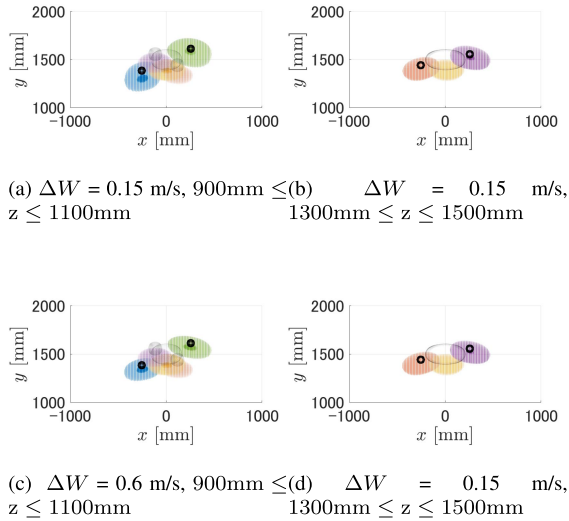


Fig. 15. Reconstruction images produced by the proposed RMA, where the width of the Doppler velocity decomposition is changed.

figures demonstrate that our proposed method maintains its reconstruction accuracy even in considerably lower SNR situation at -10 dB SNR. As a quantitative criterion for assessing the noise reduction effect of each reconstruction image, the following criterion, namely, the normalized root mean square

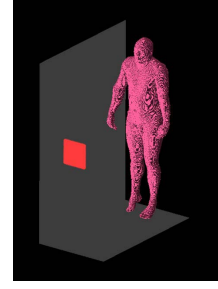


Fig. 16. Observation and target model, using realistic human numerical model in the 3-D FDTD simulation.

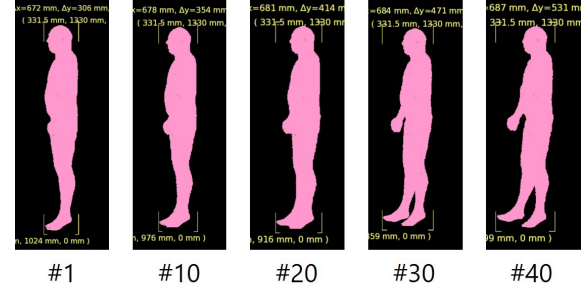


Fig. 17. Human walking postures at each pulse hit.

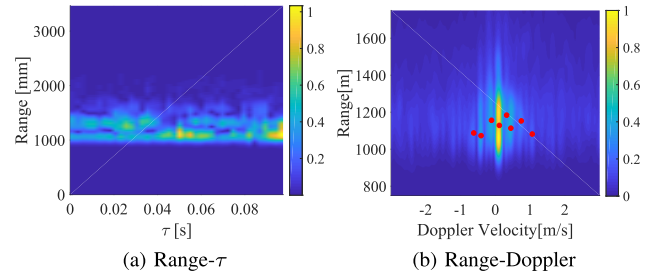


Fig. 18. Range- τ and Range-Doppler profiles in noiseless case. Red solid circles in (b) denote the extracted local maxima ($R_i, v_{d,i}$).

error (NRMSE) is introduced similar to reference [26]:

$$\text{NRMSE} = \sqrt{\frac{\iint_{\Omega} |I_{\text{orig}}(x, y, z, \tau) - \hat{I}(x, y, z, \tau)|^2 dx dy dz}{\iint_{\Omega} |I_{\text{orig}}(x, y, z, \tau)|^2 dx dy dz}} \quad (19)$$

where $I_{\text{orig}}(x, y, z, \tau)$ and $\hat{I}(x, y, z, \tau)$ denote the original and reconstruction complex-valued images, and Ω denotes the spatial area including a target. Table II lists the results of NRMSE evaluations for different SNR levels. These data demonstrates that our proposed RMA retains its reconstruction accuracy even at low SNR, and significantly enhances the noise reduction effects, compared with the images obtained in the original SNR, especially for an SNR lower than 0 dB. This is because our method is based on a coherent integration process in Doppler velocity decomposition; the coherent averaging effect and the filtering processing of an unnecessary response provided us high-level noise-robust feature, which is one of the most distinct advantages over other methods, such as the Capon filter.

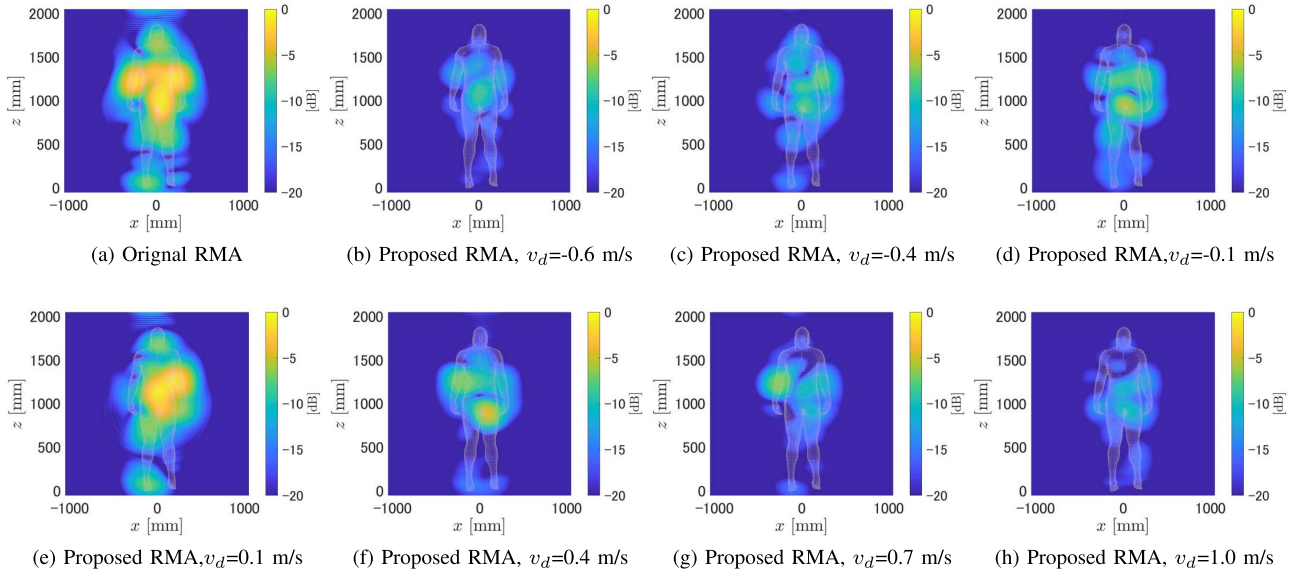


Fig. 19. Reconstruction results by the original RMA and the proposed RMA in $\text{SNR} = \infty$, at the cross-section plane $y = 1100$ mm using each Doppler velocity decomposed data. White dots denote actual target profiles.

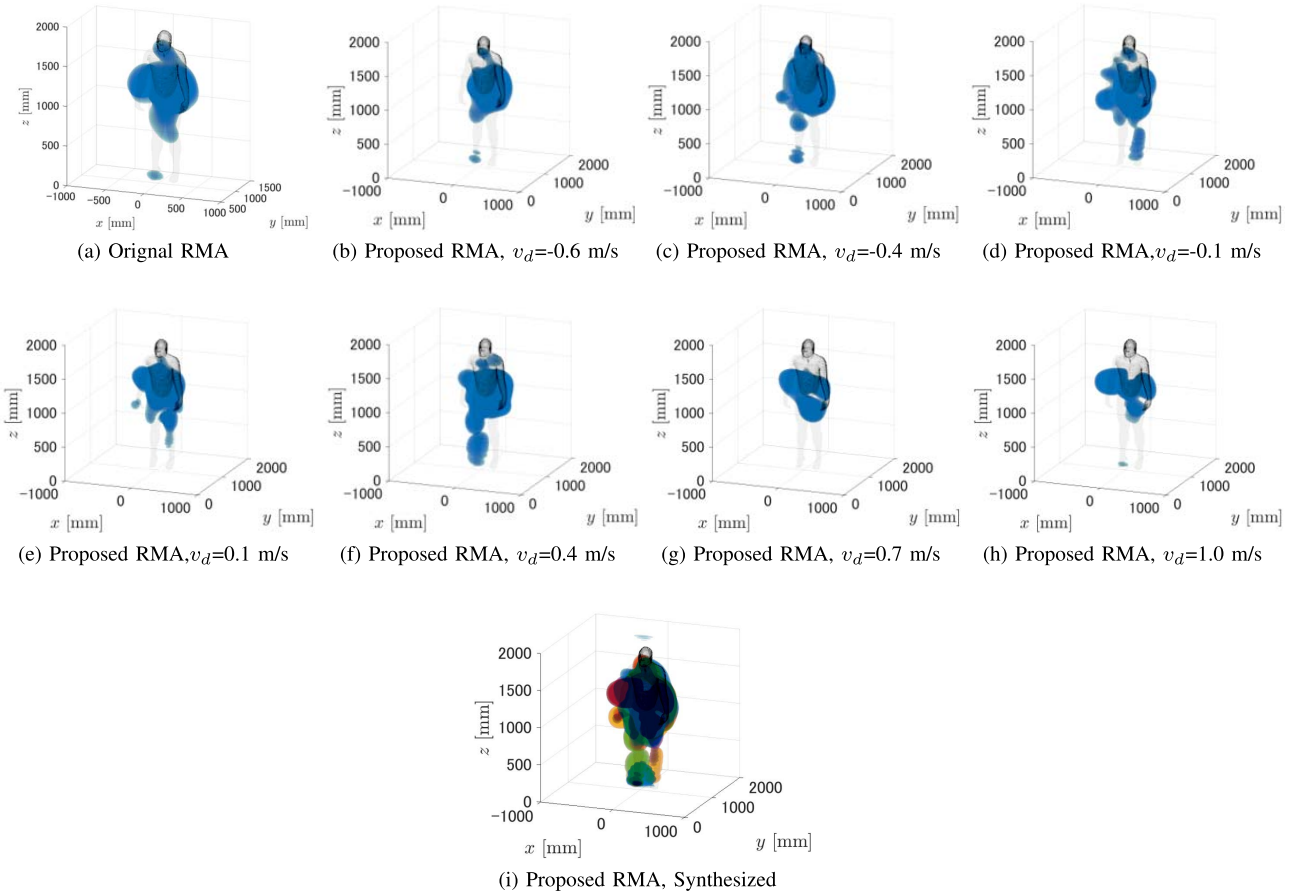


Fig. 20. 3-D Reconstruction results by the original RMA and the proposed RMA in $\text{SNR} = \infty$, using each Doppler velocity decomposed data. Black dots denote actual target profiles.

4) Sensitivity to Window Function: We describe the findings of the sensitivity analysis of the window function, *i.e.*, how the width of the window for the Doppler velocity decomposi-

tion $W(X_T, Z_T, X_R, Z_R, R, v_d; \tilde{R}_i, \tilde{v}_{d,i})$ affects the imaging performance by the proposed method. As described in the previous subsection, the width of Hamming window was set

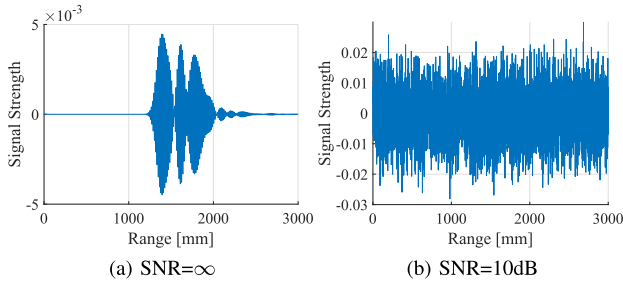


Fig. 21. Received signal without and with additive noise at SNR = 0 dB.

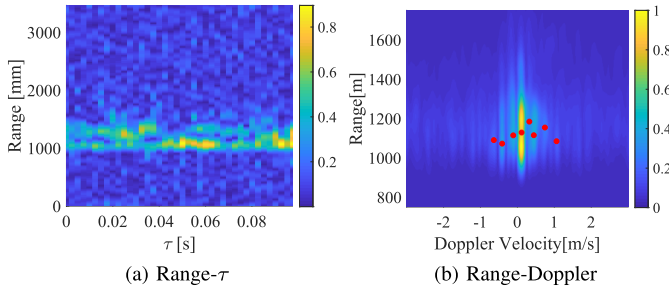


Fig. 22. Range- τ and Range-Doppler profiles in SNR = 0 dB. Red solid circles denote the extracted local maxima ($\hat{R}_i, \hat{v}_{d,i}$).

TABLE II
NRMSE FOR EACH SNR LEVEL IN THE SIMPLIFIED
HUMAN BODY MODEL

SNR	Original RMA	Proposed RMA
20 dB	0.0351	0.0139
10 dB	0.1273	0.0431
0 dB	0.3991	0.1417
-10 dB	1.1233	0.4549
-20 dB	3.8818	1.5713

TABLE III
COMPARISON OF PROCESSING TIMES REQUIRED BY EACH METHOD

Methods	SAR	RPM	Original RMA	Proposed RMA
Processing time	1430 s	60 s	450 s	750 s

to 0.3 m/s, which is 10 times the nominal Doppler resolution. Figure 15 shows the imaging examples obtained by the proposed method with window widths varied to 0.15 m/s or 0.6 m/s. The noise-free case is assumed. The NRMSEs, as defined in Eq. 19 in this case, are 0.2646 at $\Delta W = 0.015$ m/s and 0.1671 at $\Delta W = 0.6$ m/s. This figure demonstrates that while the RMA responses, in the case of $\Delta W = 0.15$ m/s, expanded because of a larger windowing width size, the sensitivity to the width of the window function is not significant if this value is set to beyond the Doppler resolution.

B. Realistic Human Model

Next, we use 3D FDTD numerical simulations to investigate our method when applied to a realistic human body phantom. By considering the actual processing time of data generation of the FDTD, we selected a 10-GHz center frequency and

a 0.5-GHz bandwidth for the transmitted pulse-modulated signal. A realistic human model is shown in Fig. 16, where its dielectric profile, where the dielectric profile of the body, including skin, muscle, bone, and other tissues, is precisely modelled using the commercial software XFDTD Bio-Pro [33]. In addition, the walking motion at each pulse hit is simulated via the Varipose model. Note that only the right arm and the left leg are swung upward toward the sensors. 40 pulse hits with a 2.5 ms PRI are transmitted, and the initial and final human postures are shown in Fig. 17. Here, the unambiguous range and resolution of the Doppler velocity are estimated at 3 and 0.3 m/s, respectively. Similar to the model described in Sec.III-A, one transmitter is located at the center of the planar array on the $y = 0$ plane, where 17×17 receiver arrays are arranged with a 15 mm spacing. The range and azimuth resolutions in this case are 300 mm and 62.5 mm, respectively, at a distance of 1000 mm.

Figure 18 illustrates the range- τ and range-Doppler velocity profiles for this case, which denotes several significant responses due to different motions of the human body. Figure 19-(a) shows the reconstruction results obtained by the original RMA, and indicates that while strong responses are observed around the upper and lower torso and the right arm, other human body parts could not be clearly recognized. In contrast, the reconstruction results obtained by the proposed method are shown in Fig. 19(b)-(h) namely, seven different Doppler velocity-decomposed datasets that were processed in parallel using the RMA. These results provide more informative images, evidenced by the clear decomposition of the right arm and left leg in motion toward the sensor, depicted as a positive Doppler velocity area. Figure 20 shows the 3-D views of the reconstruction results obtained by both the original and proposed RMA methods, where the voxels with the threshold magnitude are retained in the image. Note that, Fig. 20-(i) represents the synthesized images, where each color denotes different Doppler velocities. These figures also demonstrate that our proposed method with the selected Doppler velocity, reconstructed each part of the human body, while the original RMA could not reconstruct the human body parts, such as left and right legs. Furthermore, the proposed approach provides a Doppler velocity-associated RMA image, which can enhance performance in human body motion recognition or attitude estimation issues. Compared with the results obtained using the simplified model (see Sec. III-A), the separation performance is not clearly recognized because each part of the leg or arm has a position-dependent velocity for *e.g.*, the motion velocity of each toe will be higher than that of upper thigh. However, we should note that the original RMA (Fig. 20-(a)) could not provide a scattering responses, especially for the left and right legs. In contrast, the proposed method provides distinct images of the left (+0.5 m/s) and right (0 m/s) legs, as seen in Fig. 20-(d-e) and Fig. 20-(f), respectively. In addition, the left (0 m/s) and right (+0.5 m/s) arms are separately reconstructed in Fig. 20-(d) and 20-(f), respectively, while all the images include the torso responses. These Doppler separated images could not be obtained from the original RMA. Thus, the proposed method offers more informative images of the human body.

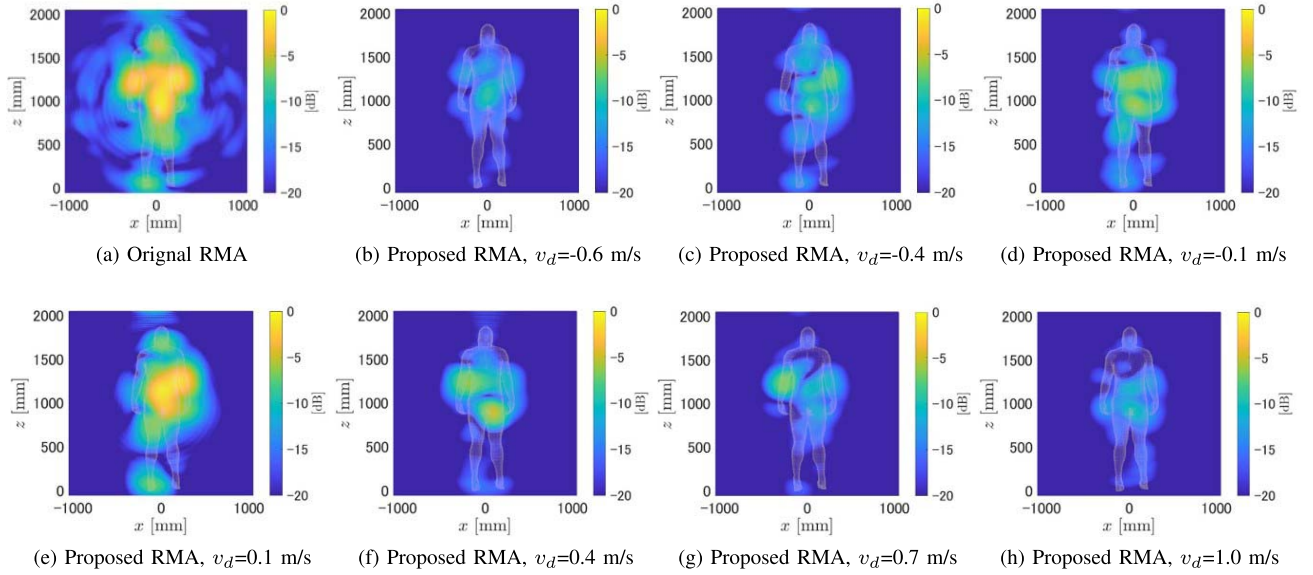


Fig. 23. Reconstruction results by the original RMA and the proposed RMA in SNR = 0 dB, at the cross-section plane $y = 1100$ mm using each Doppler velocity decomposed data. White dots denote actual target profiles.

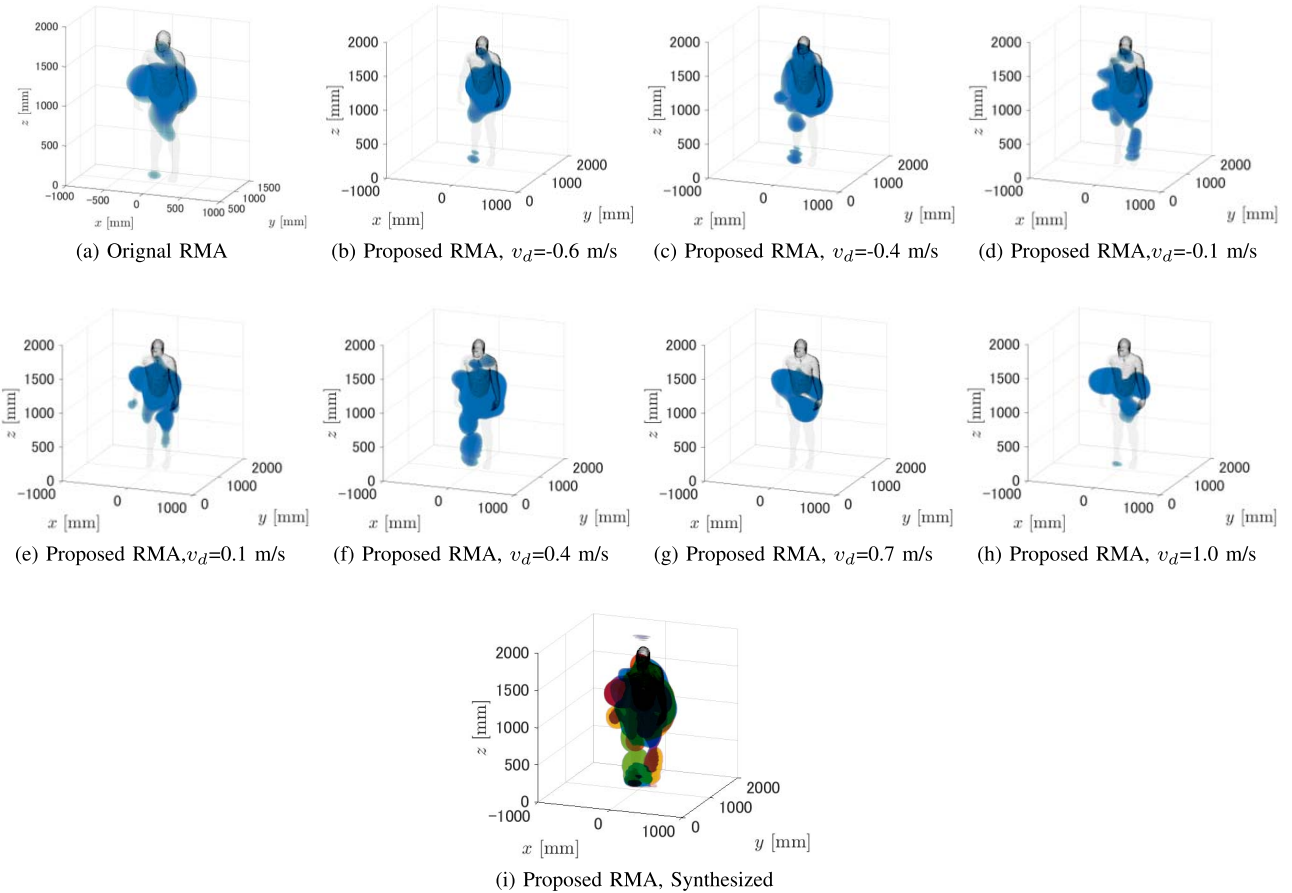


Fig. 24. 3-D Reconstruction results by the original RMA and the proposed RMA in SNR = 0 dB, using each Doppler velocity decomposed data. Black dots denote actual target profiles.

Furthermore, a case involving the presence of additive noise was investigated. Similar to the simple human body model, we tested this case with a 0 dB SNR using the same noise

model. Figure 21 shows an example of the case of the received signal with 0 dB SNR. Figure 22 illustrates the range- τ and range-Doppler profiles for this case. These results demonstrate

the presence of a significant noise component in the range- τ profile used for the original RMA and that the range-Doppler profiles are able to separate the interference of noise exhibiting a different Doppler velocity. Finally, Fig. 23 shows the original and the proposed RMA reconstruction results cross-sectioned along the $y = 1100$ mm plane, and Figure 24 shows the 3-D profiles of the reconstruction results. We thus verify the noise-robustness feature of the proposed method in a similar manner to the simplified model. The NRMSEs, as defined in Eq. 19 in this case, are 0.2027 for the original RPM and 0.1122 for the proposed RMA. These values quantitatively demonstrate the effectiveness of the proposed method in terms of noise-robustness. Note that this simulation is based on an FDTD solver with realistic shape and dielectric profiles of the human body, which provides the most accurate and reliable analysis in realistic situations.

IV. CONCLUSION

This paper introduces a Doppler velocity-associated 3-D RMA approach addressing human body imaging with walking motions to provide a multiple Doppler velocity decomposed images and noise-robustness of the original RMA. A variation of micro-Doppler components enabled us to decompose interfering responses from multiple parts of human body, which were impossible to separate in an array of smaller aperture size. In the proposed method, the Doppler separation process is first implemented in the RMA approach using a very simple algorithm, which prevents any significant increase in the computational cost. Numerical simulation tests based on either a simplified or realistic human phantom exhibiting a walking motion have demonstrated that the Doppler velocity-associated image reconstruction would provide more informative image, compared with that by the original RMA method. Furthermore, a test case including additive noise has verified that our proposed method enhances the noise-robustness feature by reducing the noise component not only in the range compression process, but also in the Doppler velocity space filtering process.

Although this paper does not report any experimental results, the numerical tests on realistic human models created by an accurate electromagnetic forward solver, *i.e.*, the FDTD method, can provide reliable results. In addition, the proposed method retained the reconstruction accuracy even at considerably low SNR ($\text{SNR} = 0$ dB). These results indicate the applicability of the real data or scenario. Furthermore, the proposed method can be extended to the MIMO array models [13], [15], [16] to obtain more accurate and noise-robust images by integrating multiple SIMO RMA images obtained by different transmitters. This method is applicable to the commercially available SIMO or MIMO radar hardware, regardless of the FMCW radar or impulse radar, because the proposed method only requires the I and Q channel data at each PRI with any array configuration. It is important to achieve phase synchronization among the MIMO or SIMO arrays to obtain accurate RMA profiles. Such synchronization can also be achieved by calibration using a simple shape target, such as a plate or corner reflector, located at a specific distance.

REFERENCES

- [1] D. A. Andrews, S. W. Harmer, N. J. Bowring, N. D. Rezgui, and M. J. Southgate, "Active millimeter wave sensor for standoff concealed threat detection," *IEEE Sensors J.*, vol. 13, no. 12, pp. 4948–4955, Dec. 2013.
- [2] O. Yurduseven, T. Fromenteze, C. Decroze, and V. F. Fusco, "Frequency-diverse computational automotive radar technique for debris detection," *IEEE Sensors J.*, vol. 20, no. 22, pp. 13167–13177, Nov. 2020.
- [3] S. Xu and A. Yarovsky, "Motion-based separation and imaging of closely spaced extended targets," *IEEE Sensors J.*, vol. 20, no. 22, pp. 13542–13551, Nov. 2020.
- [4] J. A. Nanzer and R. L. Rogers, "Human presence detection using millimeter-wave radiometry," *IEEE Trans. Microw. Theory Techn.*, vol. 55, no. 12, pp. 2727–2734, Dec. 2007.
- [5] M. Vahidpour and K. Sarabandi, "Millimeter-wave Doppler spectrum and polarimetric response of walking bodies," *IEEE Trans. Geosci. Remote Sens.*, vol. 50, no. 7, pp. 2866–2881, Jul. 2012.
- [6] Y. Kim, S. Choudhury, and H.-J. Kong, "Application of micro-Doppler signatures for estimation of total energy expenditure in humans for walking/running activities," *IEEE Access*, vol. 4, pp. 1560–1569, 2016.
- [7] Y. Li, Z. Peng, R. Pal, and C. Li, "Potential active shooter detection based on radar micro-Doppler and range-Doppler analysis using artificial neural network," *IEEE Sensors J.*, vol. 19, no. 3, pp. 1052–1063, Feb. 2019.
- [8] S. Skaria, A. Al-Hourani, M. Lech, and R. J. Evans, "Hand-gesture recognition using two-antenna Doppler radar with deep convolutional neural networks," *IEEE Sensors J.*, vol. 19, no. 8, pp. 3041–3048, Apr. 2019.
- [9] L. Du, Y. Ma, B. Wang, and H. Liu, "Noise-robust classification of ground moving targets based on time-frequency feature from micro-Doppler signature," *IEEE Sensors J.*, vol. 14, no. 8, pp. 2672–2682, Aug. 2014.
- [10] B. Gonzalez-Valdes, Y. Alvarez, S. Mantzavinos, C. M. Rappaport, F. Las-Heras, and J. Á. Martínez-Lorenzo, "Improving security screening: A comparison of multistatic radar configurations for human body imaging," *IEEE Antennas Propag. Mag.*, vol. 58, no. 4, pp. 35–47, Aug. 2016.
- [11] S. Gui, J. Li, F. Zuo, and Y. Pi, "Analysis of security imaging method for walking human screening with single channel synthetic aperture radar," *IEEE Access*, vol. 7, pp. 111363–111374, 2019.
- [12] F. Soldovieri, A. Brancaccio, G. Prisco, G. Leone, and R. Pierri, "A Kirchhoff-based shape reconstruction algorithm for the multimono-static configuration: The realistic case of buried pipes," *IEEE Trans. Geosci. Remote Sens.*, vol. 46, no. 10, pp. 3031–3038, Oct. 2008.
- [13] X. Zhuge and A. G. Yarovsky, "Three-dimensional near-field MIMO array imaging using range migration techniques," *IEEE Trans. Image Process.*, vol. 21, no. 6, pp. 3026–3033, Jun. 2012.
- [14] J. M. Lopez-Sanchez and J. Fortuny-Guasch, "3-D radar imaging using range migration techniques," *IEEE Trans. Antennas Propag.*, vol. 48, no. 5, pp. 728–737, May 2000.
- [15] Z. Wang, Q. Guo, X. Tian, T. Chang, and H.-L. Cui, "Near-field 3-D millimeter-wave imaging using MIMO RMA with range compensation," *IEEE Trans. Microw. Theory Techn.*, vol. 67, no. 3, pp. 1157–1166, Mar. 2019.
- [16] R. Zhu, J. Zhou, G. Jiang, and Q. Fu, "Range migration algorithm for near-field MIMO-SAR imaging," *IEEE Geosci. Remote Sens. Lett.*, vol. 14, no. 12, pp. 2280–2284, Dec. 2017.
- [17] L. Ding, S. Wu, P. Li, and Y. Zhu, "Millimeter-wave sparse imaging for concealed objects based on sparse range migration algorithm," *IEEE Sensors J.*, vol. 19, no. 16, pp. 6721–6728, Aug. 2019.
- [18] J. Yang, T. Jin, and X. Huang, "Compressed sensing radar imaging with magnitude sparse representation," *IEEE Access*, vol. 7, pp. 29722–29733, 2019.
- [19] M. Miller, J. Hinz, M. Saquib, and A. J. Blanchard, "Adjustable transmitter spacing for MIMO radar imaging with compressed sensing," *IEEE Sensors J.*, vol. 15, no. 11, pp. 6671–6677, Nov. 2015.
- [20] F.-F. Gu, Q. Zhang, L. Chi, Y.-A. Chen, and S. Li, "A novel motion compensating method for MIMO-SAR imaging based on compressed sensing," *IEEE Sensors J.*, vol. 15, no. 4, pp. 2157–2165, Apr. 2015.
- [21] T. Sakamoto and T. Sato, "A target shape estimation algorithm for pulse radar systems based on boundary scattering transform," *IEICE Trans. Commun.*, vol. E87-B, no. 5, pp. 1357–1365, May 2004.
- [22] S. Kidera, T. Sakamoto, and T. Sato, "High-resolution and real-time three-dimensional imaging algorithm with envelopes of spheres for UWB radars," *IEEE Trans. Geosci. Remote Sens.*, vol. 46, no. 11, pp. 3503–3513, Nov. 2008.

- [23] S. Kidera, T. Sakamoto, and T. Sato, "Accurate UWB radar three-dimensional imaging algorithm for a complex boundary without range point connections," *IEEE Trans. Geosci. Remote Sens.*, vol. 48, no. 4, pp. 1993–2004, Apr. 2010.
- [24] S. Kidera, T. Sakamoto, and T. Sato, "Super-resolution UWB radar imaging algorithm based on extended capon with reference signal optimization," *IEEE Trans. Antennas Propag.*, vol. 59, no. 5, pp. 1606–1615, May 2011.
- [25] Z. Xu, C. J. Baker, and S. Pooni, "Range and Doppler cell migration in wideband automotive radar," *IEEE Trans. Veh. Technol.*, vol. 68, no. 6, pp. 5527–5536, Jun. 2019.
- [26] S. S. Ram and A. Majumdar, "High-resolution radar imaging of moving humans using Doppler processing and compressed sensing," *IEEE Trans. Aerosp. Electron. Syst.*, vol. 51, no. 2, pp. 1279–1287, Apr. 2015.
- [27] Y. Sasaki, F. Shang, S. Kidera, T. Kirimoto, K. Saho, and T. Sato, "Three-dimensional imaging method incorporating range points migration and Doppler velocity estimation for UWB millimeter-wave radar," *IEEE Geosci. Remote Sens. Lett.*, vol. 14, no. 1, pp. 122–126, Jan. 2017.
- [28] Y. Akiyama and S. Kidera, "Low complexity algorithm for range-point migration-based human body imaging for multistatic UWB radars," *IEEE Geosci. Remote Sens. Lett.*, vol. 16, no. 2, pp. 216–220, Feb. 2019.
- [29] R. H. Stolt, "Migration by Fourier transform," *Geophysics*, vol. 43, no. 1, pp. 23–48, Feb. 1978.
- [30] A. Papoulis, *Systems and Transforms With Applications in Optics*. New York, NY, USA: McGraw-Hill, 1968.
- [31] V. U. Zavorotny and A. G. Voronovich, "Comparison of geometric optics and diffraction effects in radar scattering from steep and breaking waves," in *Proc. IEEE Int. Geosci. Remote Sens. Symp. (IGARSS)*, Jul. 2007, pp. 1350–1353.
- [32] Y. Akiyama, T. Omori, and S. Kidera, "K-space decomposition based three-dimensional imaging with range points migration for millimeter wave radar," *IEEE Trans. Geosci. Remote Sens.*, early access, vol. 60, 2021.
- [33] C. Gabriel, "Compilation of the dielectric properties of body tissues at RF and microwave frequencies," Air Force Materiel Command, Brooks Air Force Base, San Antonio, TX, USA, Tech. Rep. AL/OE-TR-1996-0037, 1996.



Tomoki Ohmori received the B.E. degree in communication engineering and informatics from the University of Electro-Communications, Tokyo, Japan, in 2019, and the M.E. degree from the Graduate School of Informatics and Engineering, University of Electro-Communications, in 2021. He joined Tohoku Electric Power Company Inc., Japan, in 2021.



Shouhei Kidera (Member, IEEE) received the B.E. degree in electrical and electronic engineering and the M.I. and Ph.D. degrees in informatics from Kyoto University, Kyoto, Japan, in 2003, 2005, and 2007, respectively. He has been with the Graduate School of Informatics and Engineering, University of Electro-Communications, Tokyo, Japan, since 2009, where he is currently an Associate Professor. He has been stayed at the Cross-Disciplinary Electromagnetics Laboratory, University of Wisconsin–Madison, as a Visiting Researcher, in 2016. From 2017 to 2021, he was a Principal Investigator of the PRESTO Program of Japan Science and Technology Agency (JST). His current research interest includes advanced radar signal processing or electromagnetic inverse scattering issue for ultra wideband (UWB) three-dimensional sensor or bio-medical applications. He is a Senior Member of the Institute of Electronics, Information, and Communication Engineers of Japan (IEICE). He is a member of the Institute of Electrical Engineering of Japan (IEEJ) and the Japan Society of Applied Physics (JSAP). He was a recipient of the 2012 Ando Incentive Prize for the Study of Electronics, the 2013 Young Scientist's Prize by the Japanese Minister of Education, Culture, Sports, Science and Technology (MEXT), and the 2014 Funai Achievement Award.